AIAA JOURNAL
Vol. 40, No. 8, August 2002

Numerical Investigation of the Turbulent Mixing Performance of a Cantilevered Ramp Injector

Bernard Parent* and Jean P. Sislian†
University of Toronto, Downsview, Ontario M3H 5T6, Canada
and
Jurgen Schumacher‡
Honeywell Engines, Phoenix, Arizona 85072

An injector geometry is considered for fuel delivery in a high-enthalpy, high-Mach-number airflow typical of that found in hypersonic propulsion systems such as the scramjet and shock-induced combustion ramjet or shcramjet. It is thought to embody the characteristics of both conventional ramp and low-angle wall injection techniques. The objective is to investigate the turbulent hypervelocity fuel/air mixing characteristics of the considered injector geometry, with particular emphasis on the effect of the convective Mach number and global equivalence ratio on its mixing efficiency. The analysis of the three-dimensional hypervelocity mixing flow is based on the Favre-averaged Navier–Stokes equations closed by the Wilcox $k\omega$ turbulence model for a multispecies gas. A Roe scheme turned second-order accurate through a symmetric total-variation-diminishinglimiter is used for the spatial discretization while approximate factorization is used to iterate in pseudotime. Obtained results show that the mixing efficiency varies by 31% for a convective Mach number ranging from 0 to 1.5 while the associated mass averaged stagnation pressure varies by only 10%. The mixing efficiency is shown to be increased by 30% for a threefold increase in the global equivalence ratio.

Nomenclature

A, B, C	=	Jacobian of F, G, S with respect to Q
c	=	mass fraction
d	=	number of dimensions
E	=	total energy, $e + k + q^2/2$
e	=	internal energy
F	=	inviscid flux vector
G	=	vector of diffusion variables
h_k	=	enthalpy of species k
J	=	metric Jacobian
K	=	diffusion matrix
k	=	turbulence kinetic energy (TKE)
M	=	Mach number
M_c	=	convective Mach number
M_t	=	turbulent Mach number, $\sqrt{(2k)}/a$
n_s	=	number of species
P	=	pressure
P_k	=	production of TKE
Q	=	vector of conserved variables
q	=	magnitude of the velocity vector
R	=	residual
R_Δ	=	discretized residual
r	=	mesh dimensions factor
S	=	vector of source terms
T	=	temperature
V	=	contravariant velocity
v	=	velocity
X	=	curvilinear coordinate
$X_{i,j}$	=	$\partial X_i/\partial x_j$
x	=	Cartesian coordinate
y^+	=	nondimensional wall distance, $y/\mu\sqrt{\rho\tau_w}$
$\Delta\tau$	=	local pseudo time step
δ_{ij}^{Kr}	=	Kronecker delta
ε	=	dissipation rate of the TKE
η_m	=	mixing efficiency
μ, κ, ν	=	viscosity, thermal conductivity and mass diffusion coefficient
ξ	=	convergence threshold
ρ	=	density
ϕ	=	equivalence ratio
ϕ_g	=	global equivalence ratio
ω	=	dissipation rate per unit of TKE

Subscripts

t	=	turbulent
w	=	wall
∞	=	freestream

Superscripts

$\star$	=	sum of the molecular and turbulent counterparts
$\circ$	=	stagnation

Introduction

AMONG the many challenges that impede the technical implementation of hypersonic airbreathing propulsion systems, like the supersonic combustion ramjet (the scramjet) and the shock-induced combustion ramjet (the shcramjet), the task of homogeneously mixing fuel and air in the high-speed, high-enthalpy flow is perhaps the most crucial. The need to inject fuel parallel to the surrounding freestream direction in order to recover the thrust caused by the momentum of the fuel (which can be appreciable at very high flight Mach numbers as stated in Ref. 1) is balanced by the need of adequate fuel penetration in the incoming air while avoiding hard-to-cool intrusive parts. This prompted the development of mixing configurations aimed at enhanced fuel penetration and fuel/air contact surface stretching (see a recent review in Ref. 2 and other mixing strategies in Refs. 3 and 4). One mixing strategy that has enjoyed considerable success is by organized longitudinal (or axial) vortices, generated either through wall-mounted ramp injectors[5–8] or low-angled wall jet injection.[9,10]

Received 7 June 2001; revision received 22 February 2002; accepted for publication 26 February 2002.

*Graduate Student, Institute for Aerospace Studies; bernard.parent@utoronto.ca. Student Member AIAA.

†Professor, Institute for Aerospace Studies; sislian@caius.utias.utoronto.ca. Associate Fellow AIAA.

‡Senior Engineer, Combustion and Emissions Department; jurgen.schumacher@honeywell.com.

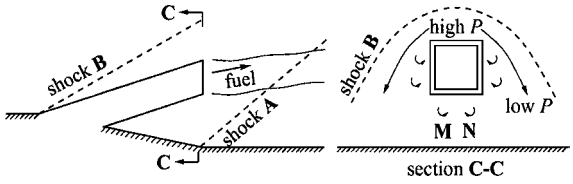

Fig. 1 Cantilevered ramp injector schematics.

In the present investigation an injection geometry is considered that is thought to embody the characteristics of both injection techniques (Fig. 1). It is referred to as a cantilevered ramp injector. Shock **B** is responsible for the cross-stream shear and shock **A** for the baroclinic effect, both of which generate strong longitudinal vortices. In addition to the side-wall vortices generated by the cross-stream shear, strong vortices will be produced behind the bluff body of the injector (vortices **M** and **N** in Fig. 1), as in the case of a low-angle wall fuel injector. These vortices will further enhance the mixing process. Unlike the low-angled wall injection and the ramp injector cases where fuel is injected in the vicinity of the bottom-wall boundary layer, the cantilevered ramp injector completely envelops and shields the fuel jet from the hypersonic boundary layer in which the maximum temperature is above the hydrogen-air ignition point. Although it can be considered as a candidate for fuel injection in scramjet combustors, the proposed cantilevered ramp injector is primarily considered for use in shock-induced combustion ramjets (shcramjets), where fuel/air mixing should take place without combustion up to a specific location in the engine.

The mechanism of vortex mixing can be considered to consist of two steps[11]: 1) a stretching of the fuel/air contact surface by the large-scale axial vortices (which is purely an inviscid effect) and 2) the spreading of the fuel/air interface through turbulence. The large-scale axial vortices can be predicted with good resolution with present numerical methods solving for the Euler equations, in contrast to the turbulent eddies (responsible for the spreading of the fuel/air interface), which require modeling. Simple algebraic turbulence models (Cebeci–Smith and Baldwin–Lomax) were used in almost all previous turbulent hypervelocity fuel/air mixing studies, with the exception of a few[12–14] where "universal" two-equation $k\varepsilon$, $k\omega$, or $q\omega$ turbulence models were considered. In the present work the Favre-averaged equations are closed by the $k\omega$ two-equation turbulence model of Wilcox.[15] Among the various existing compressibility corrections,[16–18] only the "dilatational dissipation" correction term of Wilcox[19] is retained in the present investigation because of a lack of experimental data justifying the presence of other terms. The use of the dilatational dissipation is particularly important to predict this flowfield accurately because of the high convective Mach number[11] in use.

The objective of the present investigation is to predict accurately the turbulent hypervelocity fuel/air mixing characteristics of the proposed cantilevered ramp injector, with emphasis on the effect of the convective Mach number and global equivalence ratio. At this stage of the investigation, combustion effects on the mixing performance of such injectors are ignored. Because these injectors are primarily aimed for use in shcramjet flowfields, where mixing should occur without combustion, pressure gradients around the fuel jet exit are kept low (by matching the fuel and air pressures at the fuel exit planes) in order to avoid premature ignition caused by local shocks.

Governing Equations

The Favre-averaged Navier–Stokes equations closed by the $k\omega$ turbulence model of Wilcox[15] are here expressed in generalized coordinates as $\partial Q/\partial\tau = -R$ with the residual

$$R = \sum_{i=1}^{d}\left[\frac{\partial F_i}{\partial X_i} - \sum_{j=1}^{d}\frac{\partial}{\partial X_i}\left(K_{ij}\frac{\partial G}{\partial X_j}\right)\right] - S \tag{1}$$

of which a minimization is sought. Because of the nonlinearity of the equations, the fictitious unsteady term $\partial Q/\partial\tau$ is necessary to obtain the right physical root by marching in pseudotime. For the conservative variable, convective flux, and diffusion term, we have

$$Q = \frac{1}{J}\begin{bmatrix}\rho_1\\ \vdots\\ \rho_{n_s}\\ \rho v_1\\ \vdots\\ \rho v_d\\ \rho E\\ \rho k\\ \rho\omega\end{bmatrix} \quad F_i = \frac{1}{J}\begin{bmatrix}\rho_1 V_i\\ \vdots\\ \rho_{n_s} V_i\\ \rho v_1 V_i + X_{i,1}P^\star\\ \vdots\\ \rho v_d V_i + X_{i,d}P^\star\\ V_i(\rho E + P^\star)\\ \rho V_i k\\ \rho V_i\omega\end{bmatrix} \quad G = \begin{bmatrix}c_1\\ \vdots\\ c_{n_s}\\ v_1\\ \vdots\\ v_d\\ T\\ k\\ \omega\end{bmatrix} \tag{2}$$

The total energy E and effective pressure $P^\star$ include molecular and turbulent properties, $E = e + k + \frac{1}{2}q^2$ and $P^\star = P + \frac{2}{3}\rho k$, with v_i the velocity component in the Cartesian x_i direction. The internal energy, enthalpy, and specific heat at constant pressure are determined from temperature-dependent polynomials from McBride and Reno,[20] whereas P is found through the ideal gas law from the temperature and the density. The diffusion matrix can be shown to correspond to

$$K_{ij} = \frac{1}{J}\begin{bmatrix}
\nu_1^\star\alpha_{ij} & \cdots & 0 & 0 & \cdots & 0 & 0 & 0 & 0\\
\vdots & \ddots & \vdots & \vdots & \ddots & \vdots & \vdots & \vdots & \vdots\\
0 & \cdots & \nu_{n_s}^\star\alpha_{ij} & 0 & \cdots & 0 & 0 & 0 & 0\\
0 & \cdots & 0 & \mu^\star\beta_{ij}^{11} & \cdots & \mu^\star\beta_{ij}^{1d} & 0 & 0 & 0\\
\vdots & \ddots & \vdots & \vdots & \ddots & \vdots & \cdots & \vdots & \vdots\\
0 & \cdots & 0 & \mu^\star\beta_{ij}^{d1} & \cdots & \mu^\star\beta_{ij}^{dd} & 0 & 0 & 0\\
\nu_1^\star\alpha_{ij}h_1 & \cdots & \nu_{n_s}^\star\alpha_{ij}h_{n_s} & \mu^\star\sum_k\beta_{ij}^{k1}v_k & \cdots & \mu^\star\sum_k\beta_{ij}^{kd}v_k & \kappa^\star\alpha_{ij} & \mu_k^\star\alpha_{ij} & 0\\
0 & \cdots & 0 & 0 & \cdots & 0 & 0 & \mu_k^\star\alpha_{ij} & 0\\
0 & \cdots & 0 & 0 & \cdots & 0 & 0 & 0 & \mu_\omega^\star\alpha_{ij}
\end{bmatrix} \tag{3}$$

where α and β are function of the metrics only, $\alpha_{ij} = \Sigma_{k=1}^{d} X_{i,k}X_{j,k}$ and $\beta_{ij}^{mn} = \alpha_{ij}\delta_{mn}^{Kr} + X_{j,m}X_{i,n} - \frac{2}{3}X_{j,n}X_{i,m}$. For the effective viscosity, thermal conductivity, mass diffusion, and diffusion coefficients of the turbulence kinetic energy (TKE) and length scale determining equations, we set $\mu^\star = \mu + \mu_t$, $\kappa^\star = \kappa + C_P(\mu_t/Pr_t)$, $\nu_k^\star = \nu_k + (\mu_t/Sc_t)$, $\mu_k^\star = \mu + \mu_t/\sigma_k$, and $\mu_\omega^\star = \mu + \mu_t/\sigma_\omega$. The molecular diffusion coefficients μ, κ, and ν for each species are determined from polynomials based on the kinetic theory of gases.[21] The viscosity and mass diffusion of the gas mixture are found from Wilke's mixing rule, whereas the thermal conductivity of the mixture is determined from the Mason and Saxena relation. The source term includes the baseline terms of the $k\omega$ model as well

as some additional terms needed to account for compressibility effects:

$$S = \frac{1}{J}\begin{bmatrix} \vdots \\ 0 \\ P_k - \rho\varepsilon - \rho\varepsilon f(M_t) \\ \dfrac{\omega}{k}\left(\dfrac{5}{9}P_k - \dfrac{5}{6}\rho\varepsilon\right) + \rho\omega^2 f(M_t) \end{bmatrix} \tag{4}$$

where $\omega \equiv \varepsilon/k$. The dilatational dissipation correction terms [that is, the ones involving $f(M_t)$] are necessary to account for the reduced growth of shear layers when the convective Mach number is high.[11,22] The Wilcox[19] dilatational dissipation model specifies $f(M_t)$ as $f(M_t) = \frac{3}{2}\max(0, M_t^2 - \frac{1}{16})$. This improves the baseline $k\omega$ equations in solving high convective Mach-number shear layers without under predicting the skin friction in high-Mach-number boundary layers, at least up to a freestream Mach number of 6. More compressibility corrections exist,[16–18] but because of very few or no empirical data to justify their presence their effect is neglected in the present study. Based on dimensional analysis arguments, the turbulent viscosity μ_t can be written as $\mu_t = 0.09\ (\rho k/\omega)$ from which the effective viscosity can be determined as $\mu^\star = \mu + \mu_t$. From the exact form of the transport equation for k, the turbulence kinetic energy production term can be written in generalized coordinates as

$$P_k = \sum_{i=1}^{d}\sum_{j=1}^{d}\left(-\frac{2}{3}\rho k X_{i,j}\frac{\partial v_j}{\partial X_i} + \sum_{m=1}^{d}\sum_{n=1}^{d}\mu_t \beta_{ij}^{mn}\frac{\partial v_m}{\partial X_i}\frac{\partial v_n}{\partial X_j}\right) \tag{5}$$

where $\mu^\star$ is substituted to μ_t to avoid giving k a nonzero value at the inflow as a means of initiating turbulence. Finally, the turbulent Prandtl number, σ_k, and σ_ω are set to 0.9, 2.0, and 2.0, respectively, while the turbulent Schmidt number is set to 1.0, unless otherwise indicated.

Discretization and Integration

All partial derivatives are discretized using centered finite difference second-order-accurate stencils except for the convection derivative, which is discretized using the approximate Riemann solver of Roe[23] and made second-order accurate through a symmetric minmod limiter by Yee et al.[24] The discretized residual is solved to steady state using a block-implicit approximate factorization algorithm[25,26] and a linearization strategy of the viscous terms by Chang and Merkle[27]:

$$\prod_{i=1}^{d}\left[I + \Delta\tau\overline{\delta_{X_i}A_i} - \Delta\tau C_i^- - \Delta\tau\sum_{j=1}^{d}\delta_{X_i}\left(K_{ij}\delta_{X_j}B\right)\right]\Delta Q = -\Delta\tau R_\Delta \tag{6}$$

with B the linearization Jacobian of the viscous terms ($B \equiv \partial G/\partial Q$) and C_i^- the linearization Jacobian of the negative source terms ($\partial S^-/\partial Q$) for the $i = 1$ sweep but ignored for the other sweeps. Only the negative source terms are linearized to ensure the stability of the implicit algorithm.[28] The term $\overline{\delta_{X_i}A_i}$ is symbolic and stands for the linearization of the first-order Roe scheme with the Roe Jacobian locally frozen.[29,30] Although more costly per iteration compared to an LUSGS inversion strategy, approximate factorization is chosen here for its ability to solve the Roe scheme without the need of introducing an explicit artificial dissipation term in the residual (the entropy correction) to stabilize the iterative process. As shown in a subsequent section, the introduction of the entropy correction can lead to excessive artificial dissipation, which affects the accuracy of the solution considerably.

Convergence is reached when ξ for all nodes falls below a user-defined threshold value ξ_{verge}. We choose to define ξ as the summation of the discretized continuity residuals weighted by J^{-1} and the density:

$$\xi \equiv \frac{J}{\rho}\sum_{k=1}^{n_s}|R_{\Delta_k}| \tag{7}$$

The pseudo time step $\Delta\tau$ is fixed to the geometric average between the minimum and maximum Courant–Friedrichs–Lewy (CFL) conditions, which is found to give faster convergence than the minimum CFL condition for cases involving high mesh aspect ratios.

Boundary Conditions

Finite difference boundary conditions can be enforced on any node of the computational domain, and some computational subzones can be turned off at will, making the solution of complicated flow geometries possible while avoiding a multiblock formulation. Zeroth-order extrapolation polynomials are used to obtain the properties from the adjacent inner node at the supersonic outflow boundary, whereas the properties at the supersonic inflow boundary node are not altered in pseudotime. As suggested by Wilcox,[31] the specific dissipation rate is set to $10\,q_\infty/L$ in the freestream, with L here equal to one meter. At the symmetry node a first-order extrapolation is used to obtain $P^\star$, k, ω, ρ and the velocity components tangent to the surface, while the perpendicular velocity component is set to zero. At the wall the turbulence kinetic energy and the velocity are fixed to zero, while the effective pressure is extrapolated using a first-order polynomial. Also, the dissipation rate at the wall is specified as $\omega_w = \frac{36}{5}(\mu/\rho d_w^2)$ with d_w the distance between the near-wall node and the wall.[31]

Validation

A Mach 2 swept ramp injector mixing problem is studied experimentally and numerically in Donohue et al.[32] Because of the advanced measuring technique utilized, the experimental results include the contours of many flow properties of interest at different cross-stream planes and serve as an excellent test bed for validating our numerical method. Mixing takes place in a 30-mm-deep and 18.1-mm-high duct using the swept injector design shown in Fig. 2. A grid composed of 2.4 million nodes is judged sufficient for this problem as it gives mass fraction contours of the injectant close to those obtained using a 0.33-million-node mesh. To simulate the 2-mm-high incoming boundary layer present in the experiments, a short constant-area duct is concatenated to the injector domain. A rectangular-shaped injectant jet (as opposed to a circular-shaped jet) is used in the numerical simulations to simplify the gridding process. The duct walls at $y = \pm 15.2$ mm are simulated as symmetry planes in order to concentrate the nodes in the mixing region. The incoming air is set to a pressure of 30.8 kPa, a temperature of 163 K, and a Mach number of 2, while the injectant inflow is fixed to a speed of 470 m/s, a temperature of 180 K, and a mass flux of 0.00261 kg/s. Particular attention is given to matching the injectant speed and mass flow rate between the experiments and numerical simulation, as these two parameters are shown subsequently to influence the mixing process significantly. Also, a short constant area runway of 2 mm is imposed to the injectant prior to injection. The Wilcox $k\omega$ model is used in conjunction with the Wilcox dilatational dissipation correction, yet compressibility effects play a minimal role in this case. An additional simulation with no dilatational dissipation modeling showed a relative decrease of only 15% in the maximum injectant mole fraction at $x = 40$ mm. Figure 3 shows a comparison between the injectant mole fraction contours obtained experimentally and with the present numerical method in the planes $x = 2.5$, 10, and 40 mm. At a turbulent Schmidt number of 0.25, the agreement is excellent both on the basis of the shape and

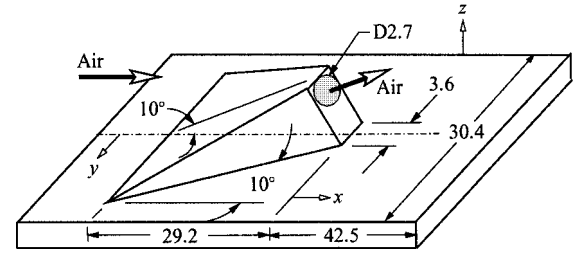

Fig. 2 Schematic of the Donohue swept ramp injector; all dimensions are in millimeters unless otherwise specified.

Table 1 Test cases

					Hydrogen inflow conditions				
Case	M_c	Δq, m/s	ϕ_g	Sc_t	q, m/s	ρ, kg/m^3	T, K	M	T°, K
C1	−0.5	−715	1	1	2613	0.006787	170	2.63	407
C2	0	0	1	1	3328	0.005317	217	2.97	600
C3	0.5	844	1	1	4172	0.004242	272	3.33	875
C4	1	1815	1	1	5143	0.003434	336	3.7	1252
C5	1.5	2960	1	1	6288	0.002814	410	4.09	1780
C3r1	0.33	844	0.33	1	4172	0.001439	802	1.94	1405
C3r2	0.73	844	3	1	4172	0.012678	91	5.76	694
C3h	0.5	844	1	0.25	4172	0.004242	272	3.33	875

[a]Air is set to $q = 3328$ m/s, $T = 462$ K, $\rho = 0.0357$ kg/m^3, and $M = 7.73$, while $P^\star$ for air and H_2 is set to 4758 Pa.

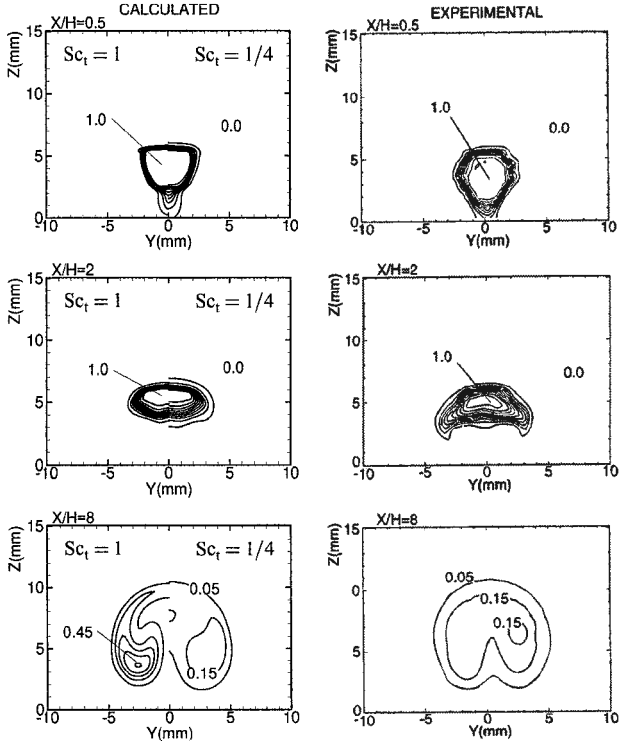

Fig. 3 Injectant mole fraction at different x stations for the Donohue injector case. H refers to the height of the injector (that is, 5 mm).

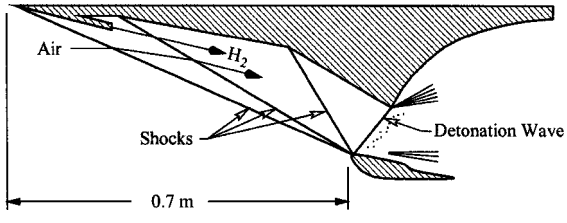

Fig. 4 External compression shcramjet schematic.

size of the region spanned by the injectant and on the basis of the injectant mole fraction quantities. However, fixing Sc_t to 1 results in underpredicted mixing and a maximum injectant mole fraction more than two times the one measured experimentally in the far field (Fig. 3). A good choice of the turbulent Schmidt number is hence shown to be critical in the correct prediction of this flowfield.

Injector Configuration

Fuel injection is assumed to take place after the first shock in the inlet of an on-design external compression shcramjet at a flight Mach number of 11 as shown in Fig. 4. The shcramjet inlet is designed assuming a flight dynamic pressure of 67 kPa, equal strength inlet shocks, a 900 K temperature prior to the detonation wave, and an inlet length of 0.7 m. This results in air properties of $P = 4758$ Pa,

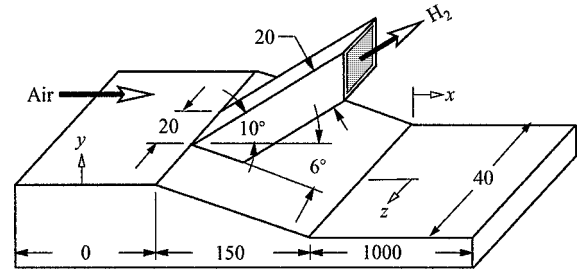

Fig. 5 Design of the cantilevered ramp injector; all dimensions are in millimeters unless otherwise noted.

$T = 462$ K, and $M = 7.73$ after the first inlet shock, which are used as inflow properties to the injector problem studied herein (Fig. 5). Whereas the fuel/air mixture would cover a distance of at most 0.8 m in the shcramjet inlet before reaching the detonation wave, the present study assumes a mixing region length of 1 m to account for the increase in mixing per unit length that is expected to occur after the second and third inlet shocks, where the flow height diminishes. The injector geometry and air inflow properties are unaltered for all test cases, and only the fuel jet conditions are varied, according to Table 1 . Except for cases C3r1 and C3r2, where the mass flux of hydrogen is varied, the fuel is injected in stoichiometric proportions with respect to the flow of air entering the shcramjet. The wall temperature is fixed in all cases to 462 K, and the inflow pressure for the air and the fuel is set to 4758 Pa.

The cases in Table 1 have the following terminology: C stands for the cantilevered injector design with the dimensions shown in Fig. 5, followed by a number related to the velocity difference between the fuel and the air. A change in the convective Mach number of the system is achieved through a variation of the stagnation temperature of the fuel. The acronyms r1 and r2 stand for cases run with three times less and three times more injected hydrogen mass flux, respectively, whereas h refers to a turbulent Schmidt number of 0.25. All other cases are run at a turbulent Schmidt number of unity. A fuel runway of 10 mm prior to injection is imposed inside the injector to avoid a singularity point in the turbulence and other flow properties at the point of injection.

All injector flowfields are computed with the Wilcox $k\omega$ model[15] including the dilatational dissipation correction of Wilcox.[19] No entropy correction term is used in conjunction with the Roe scheme to avoid excessive artificial dissipation (see the following). Second-order-accurate symmetry boundary conditions are imposed at $z = 0$ and 20 mm to simulate an infinite array of injectors along z. Inflow is specified as the top boundary condition for $x < 0$, whereas outflow is specified for $x > 0$.

The mixing efficiency is defined as the ratio between the mass flow rate of oxygen that would burn at $x = x_s$ and the mass flow rate of oxygen entering the just-mentioned shcramjet inlet (see Fig. 4) through a depth of 0.02 m:

$$\eta_m \equiv \frac{\iint \rho v_1 c^R_{O_2}\,dy\,dz\Big|_{x=x_s} + \int\int_0^{x_s} \rho v_2 c^R_{O_2}\,dx\,dz\Big|_{y=y_{top}}}{0.02726\ \text{kg/s}} \tag{8}$$

where the flow exiting the top boundary is taken into account through the second term in the numerator. It is noted that Eq. (8) does not

include the flammability limits of hydrogen/air chemistry and is hence expected to overestimate the amount of oxygen burned for some cases. The reacting mass fraction of oxygen $c^R_{O_2}$ is set to c_{O_2} if $c_{H_2} > c^S_{H_2}$ and to $c^S_{O_2} c_{H_2}/c^S_{H_2}$ otherwise. The stoichiometric mass fraction of hydrogen $c^S_{H_2}$ corresponds to 0.02876. Similarly, the integration of the mass-flux-averaged stagnation pressure includes the addition of the mass flow through the top boundary:

$$P^\circ_{\text{ave}} \equiv \frac{\iint \rho v_1 P^\circ \,\mathrm{d}y\,\mathrm{d}z\Big|_{x=x_s} + \int\int_0^{x_s} \rho v_2 P^\circ \,\mathrm{d}x\,\mathrm{d}z\Big|_{y=y_{\text{top}}}}{\iint \rho v_1 \,\mathrm{d}y\,\mathrm{d}z\Big|_{x=x_s} + \int\int_0^{x_s} \rho v_2 \,\mathrm{d}x\,\mathrm{d}z\Big|_{y=y_{\text{top}}}} \tag{9}$$

The convective Mach number is defined as the ratio between the difference between the inflow speed of fuel and the inflow speed of air and the sum of the sound speed of air and hydrogen at inflow, that is, $M_c \equiv q_{H_2} - q_{\text{air}}/a_{H_2} + a_{\text{air}}$, where q_{H_2}, q_{air}, and the sound speeds can be readily determined from Table 1. M_c is not a flow property but a property of the system, as it depends solely on the inflow properties of fuel and air.

Numerical Accuracy Assessment

Although the approximate closure of the Favre-averaged equations through turbulence modeling induces some error in the determination of the flowfield, it would be erroneous to believe this to be the only source of error present[33,34]: the convergence threshold, the grid, the wall node spacing, and the user-specified explicit artificial dissipation (that is, the entropy correction term) can all contribute to quite appreciable errors on the computed properties.

Solution Convergence

The value given to the convergence threshold ξ_{verge} is chosen for all cases to be 3×10^3 1/s. For case C3 an additional simulation at a 10-fold decrease in ξ_{verge} (that is, 3×10^2 1/s) showed small changes in the mixing efficiency, mass-flux-averaged stagnation pressure, and maximum c_{H_2} where the relative error did not exceed 0.4, 0.16, and 0.8%, respectively, at any x station.

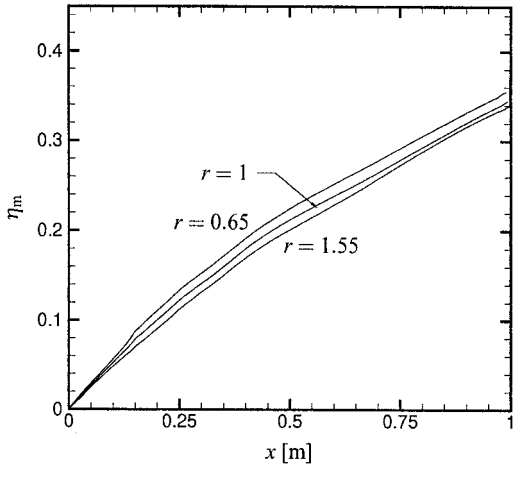

Fig. 6 Grid-convergence study of the mixing efficiency for case C3; a mesh dimensions factor of $r = 0.65$, 1.0, and 1.55 correspond to a mesh of 0.68, 2.5, and 9.3 million nodes, respectively.

Node Spacing at the Wall

Spacing at the wall is fixed for all simulations to 30 microns, which results in a value of y^+ at the wall of 1.8–2.5 in the mixing region. Even though it is usually suggested[31] to use a somewhat lower y^+ when integrating through the laminar sublayer, an additional simulation for case C3 at a wall node distance of 10 microns showed no discernible difference of boundary-layer height and wall shear stress while exhibiting a relative change in the mixing efficiency and stagnation pressure at the domain exit of only 1 and 0.5%, respectively. This is attributed to the slight grid density decrease in the mixing layer, a consequence of higher clustering at the surfaces.

Entropy Correction

Despite being a rare occurrence, a well-known deficiency of the Roe scheme is in generating aphysical phenomena in certain flowfields. This can be remedied by introducing an explicit artificial dissipation term in the discretization stencil, commonly referred to as entropy correction. All of the cases presented in this study are run without the entropy correction term to avoid excessive artificial diffusion in the boundary layers and shear layers. An additional test case, however, includes the entropy correction term of Yee et al.[24] with $\tilde{\delta} = 0.5$. Such results in a twofold increase in the bottom-wall boundary-layer thickness, increased shock smearing, as well as an increase in the mixing efficiency at the domain exit of 17%. Because no difference in the shock-wave and expansion fan patterns throughout the flowfield is observed, the stand-alone Roe scheme (with $\tilde{\delta} = 0$) is judged adequate for the problem tackled herein, and the use of the entropy correction term is avoided.

Grid Convergence

Shown in Fig. 6 is the mixing efficiency of case C3 obtained using $207 \times 121 \times 27$ ($r = 0.65$), $319 \times 187 \times 42$ ($r = 1.0$), and $494 \times 290 \times 65$ ($r = 1.55$) meshes. Each grid is built as shown in Fig. 7 with the number of grid lines in each curvilinear coordinate proportional to r. The mesh dimensions ratio between the fine and medium grids is equal to the one between the medium and coarse grids. Such a strategy, as opposed to setting a constant Δr between meshes, translates into a more rigorous grid-convergence study. Indeed, it is not hard to see that results obtained on two meshes, say, at $r = 3.0$ and 3.2 will show little difference in properties, whereas the discrepancy will be much more pronounced between results obtained at $r = 0.2$ and 0.4 because of the much higher relative change in mesh size in the latter case than in the former. It is hence desirable when comparing changes in properties between different meshes to ensure the ratio of mesh dimensions between one grid and the next to always be the same. The mixing efficiency throughout the mixing region exhibits small changes between the medium and fine grids, indicating close grid convergence. Results obtained from various similar investigations for two-dimensional planar mixing problems indicate that the absolute grid error on a $r = 1$ grid is approximately three times the difference between the solutions obtained using a

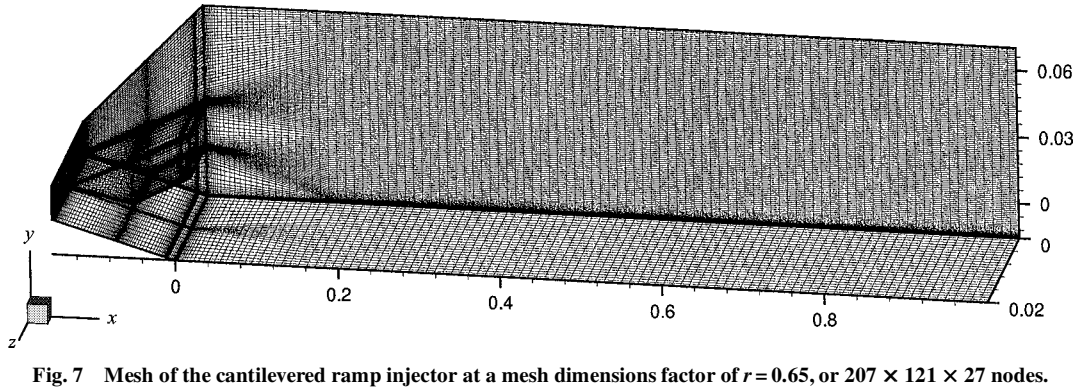

Fig. 7 Mesh of the cantilevered ramp injector at a mesh dimensions factor of $r = 0.65$, or $207 \times 121 \times 27$ nodes.

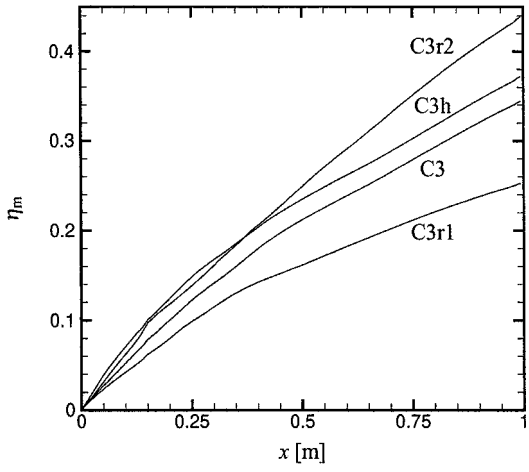

Fig. 8 Influence of the turbulent Schmidt number Sc_t and global equivalence ratio ϕ_g on the mixing efficiency; for case C3h, Sc_t is set to 0.25, while for cases C3r1 and C3r2 ϕ_g is given a value of 0.33 and 3, respectively; by default both Sc_t and ϕ_g are set to 1.

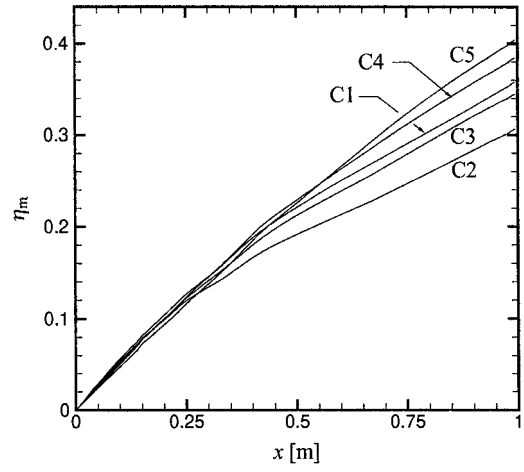

Fig. 10 Mixing efficiency of a cantilevered ramp injector for the convective Mach number range $-0.5 < M_c < 1.5$.

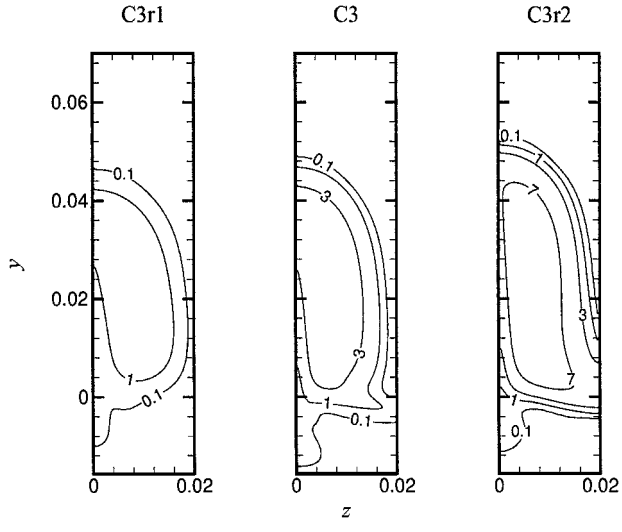

Fig. 9 Equivalence ratio contours at $x = 1.0$ m for cases C3r1, C3, and C3r2; all dimensions in meters.

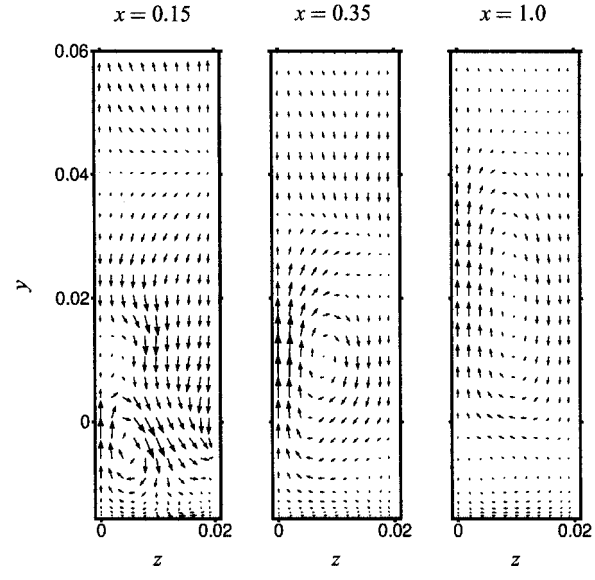

Fig. 11 Velocity vectors for the C3 case; the length of the arrows is proportional to the velocity magnitude in the yz plane, with the maximum length corresponding to 560 m/s. All dimensions in meters.

$r = 0.65$ mesh and a $r = 1$ mesh. The error on the mixing efficiency is thus estimated to be at most 0.04 units at any x station.

Turbulent Schmidt Number

Being a closure coefficient to the $k\omega$ turbulence model, the turbulent Schmidt number is flowfield dependent. Previous studies[35] of hypervelocity hydrogen/air mixing indicate that the use of a turbulent Schmidt number of 0.2–0.5 translates into better agreement with experimental data. The influence of the turbulent Schmidt number is here assessed through case C3h: an additional simulation at a convective Mach number of 0.5 with $Sc_t = 0.25$. The influence on the mixing efficiency is not too pronounced as Fig. 8 illustrates: a small relative change of 8% occurs for a fourfold decrease in Sc_t.

Results and Discussion

Global Equivalence Ratio

The amount of hydrogen injected is varied to induce a global equivalence ratio of 0.33 for case C3r1, 1.0 for case C3, and 3.0 for case C3r2. Cases C3r1 and C3r2 are referred to hereafter as the fuel-lean and fuel-rich cases. Because it is not possible to keep the same convective Mach number and speed difference Δq while altering the injected mass of hydrogen, we choose to keep Δq constant and let M_c vary (see Table 1). The parameter Δq influences the average shear-layer growth directly, whereas the change in M_c from 0.33 for case C3r1 to 0.73 for case C3r2 would influence the shear-layer growth by less than 25% (based on the Dimotakis[11] correlation for compressible shear layers). Even though the C3r2 case is handicapped by a higher convective Mach number, the mixing efficiency is shown to be 30% higher than for C3 and almost two times more at the domain exit than for the fuel-lean case (Fig. 8). A fuel-rich injection is beneficial to η_m by increasing the amount of fuel in the zones with $\phi < 1$ while not considerably affecting the amount of air burned in the fuel-rich regions; a slight local overshoot in the hydrogen required for burning is not too detrimental to the mixing efficiency because of the very low stoichiometric mass fraction of hydrogen. However, because η_m as outlined in Eq. (8) does not take into account the flammability limits of H_2–air chemistry the mixing efficiency comparison of Fig. 8 must be analyzed cautiously. The ϕ contours including the limits of flammability ($0.1 \leq \phi \leq 7$ at atmospheric pressure[36]) at the domain exit for cases C3r1, C3, and C3r2 are shown in Fig. 9. Whereas most of the area covered by the fuel is expected to burn for cases C3r1 and C3, a large portion of the mixture is too fuel rich to burn for case C3r2, which is undesirable. Consequently, a fuel-rich injection strategy is not recommended for this particular problem as the mixing process is not sufficiently fast in decreasing the hydrogen mass fraction of the mixture below the flammability upper limit. The fuel-lean injection case exhibits a lower mixing efficiency and a higher mixture temperature caused by a higher injection temperature necessary to induce a lower injected mass flux. This can be desirable if burning is desired near the injection point but undesirable if injection is intended for a shcramjet.

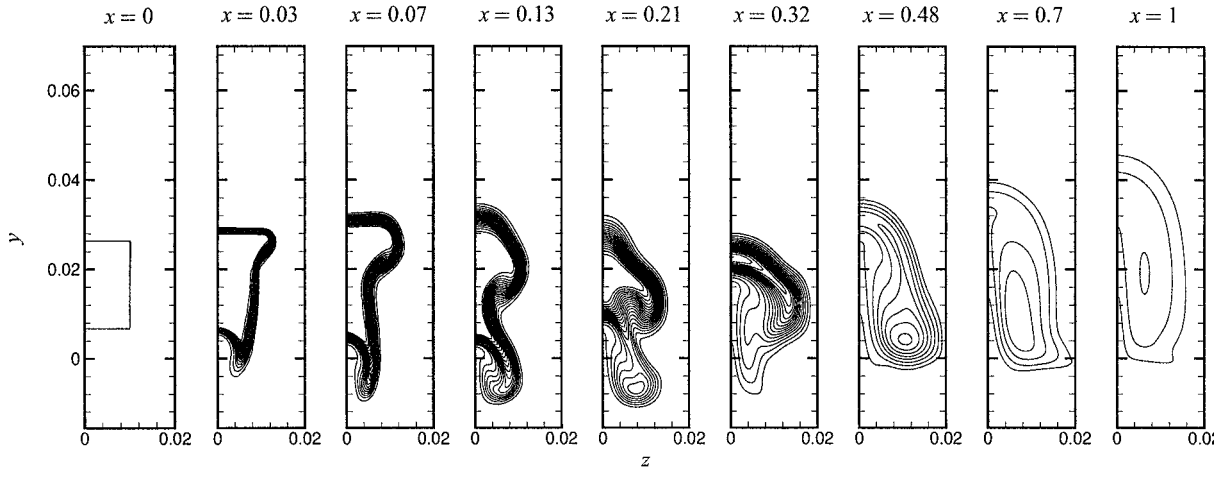

Fig. 12 Hydrogen mass fraction contours for case C3, with the contour levels starting at $c_{H_2} = 0.05$ and at every 0.05 units. All dimensions in meters.

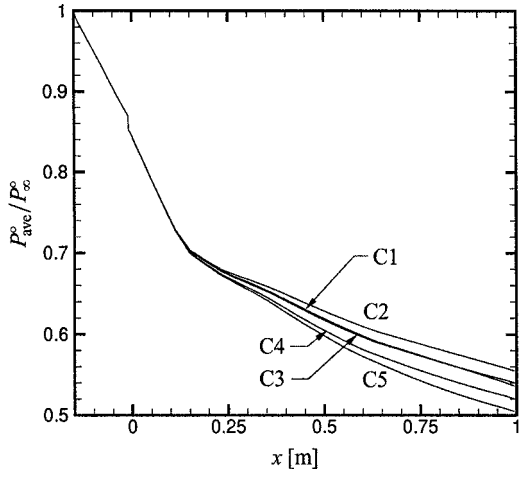

Fig. 13 Normalized mass-flux-averaged stagnation pressure for the convective Mach number range $-0.5 < M_c < 1.5$.

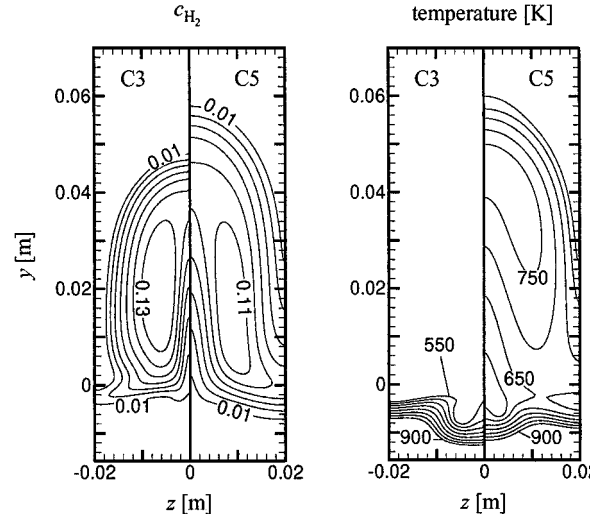

Fig. 14 Temperature and hydrogen mass fraction contours at $x = 1.0$ m for cases C3 and C5.

Therefore, the injection of hydrogen in stoichiometric proportions with the amount of air entering the domain seems to be the best alternative for this particular injector.

Convective Mach Number

An investigation of the influence on the mixing efficiency of the convective Mach number is now performed. For cases C1–C5, M_c is varied between −0.5 and 1.5, where a negative sign indicates a lower fuel speed with respect to the air. Shown in Fig. 10, the mixing efficiency exhibits a change of 31% at the domain exit from $M_c = 0$ to 1.5. A striking trait of Fig. 10 is the quasi-independence of the mixing efficiency on the convective Mach number in the near-field mixing region. This is thought to be caused by a saturation of the mixing layer growth as a result of compressibility effects as the turbulent Mach number is high. The strong axial vortices induce appreciable cross-stream velocity gradients, creating turbulence at high turbulent Mach numbers. Additional shear stresses originating from a change in velocities between the air and hydrogen do not contribute to the growth of the shear layer as the turbulence in the mixing layer is already saturated by the axial vortices. The velocity vectors of case C3 shown in Fig. 11 give a good indication of the crossflow magnitude and induced velocity gradient in the near field. However, in far field the effect of the convective Mach number is predominant on the mixing layer growth as a result of the decrease in intensity of the axial vortices (Figs. 11 and 12). Interestingly, the 31% increase in mixing translates into mass-averaged stagnation pressure losses of only 10% as shown in Fig. 13. Nevertheless, there is some concern as to the relevance of the mass-averaged stagnation pressure as a means to assess losses.

Aside from the rise in mixing efficiency, a high convective Mach number induces an appreciable increase in temperature in the mixing layer. The fuel mass fraction contours juxtaposed to the temperature contours at the domain exit for cases C3 and C5 are shown in Fig. 14. Although not shown here, for the first 60 cm of the mixing region the maximum temperature in the mixing layer exceeds the one necessary for H_2–air ignition (~900 K) for case C5 but not for cases C1, C2, and C3. Because the mixing cases studied herein are intended for use in the inlet of a shcramjet, no ignition prior to the combustor is a necessity, thus probably eliminating as viable alternatives the higher convective Mach numbers.

Conclusions

A numerical method to solve three-dimensional injector flowfields is implemented and validated. The dilatational dissipation correction of Wilcox along with the $k\omega$ model of Wilcox are deemed adequate in capturing the essentials of the flowfield physics and excellent agreement is shown with the experimental data of a swept ramp injector by Donohue et al.[32] A grid-validation study is performed, and a relative error of approximately 10% is estimated on the mixing efficiency for a 2.5-million-node grid. The use of the Yee entropy correction factor in conjunction with the Roe scheme is found to be unnecessary for the cantilevered ramp injector flowfield, and its use should be avoided because of increased artificial diffusion of the mixing layer.

The influence of the turbulent Schmidt number on the mixing efficiency is shown to be minimal: for a turbulent Schmidt number variation from 1.0 to 0.25, the mixing efficiency increases by only

8%. A fuel-rich injection is found to translate into a large portion of the mixture at the domain exit to be outside the hydrogen/air flammability limits. A fuel-lean injection reduces the mixing efficiency by 27% and induces a high mixture temperature, which is beneficial if burning is desired close to the injection point but undesirable otherwise. If burning is not desired near the point of injection, injecting the fuel at stoichiometric conditions with the incoming air is the recommended approach.

Because of the injection of the fuel away from the wall, the use of a cantilevered ramp injector design results in minimal presence of the injectant in the hot boundary layer. This is a beneficial feature if injection is intended for a shcramjet engine, where no premature ignition should occur prior to the detonation wave. The mixing efficiency of the cantilevered ramp injector is shown to be increased at the domain exit by 31% from $M_c = 0$ to 1.5 while the mass-averaged stagnation pressure decreases by only 10%. In the near-field mixing region the convective Mach number has a negligible impact on the mixing efficiency. This is thought to be related to an already saturated turbulent mixing layer growth induced by the high shear stresses originating from the axial vortices.

Acknowledgment

This work has been supported by the Natural Sciences and Engineering Research Council.

References

[1]Swithenbank, J., Eames, I. W., Chin, S. B., Ewan, B. C. R., Yang, Z., Cao, J., and Zhao, X., "Turbulent Mixing in Supersonic Combustion Systems," *High-Speed Flight Propulsion Systems*, edited by S. N. B. Murthy and E. T. Curran, Vol. 137, Progress in Aeronautics and Astronautics, AIAA, Washington, DC, 1991, Chap. 6.

[2]Gutmark, E. J., Schadow, K. C., and Yu, K. H., "Mixing Enhancement in Supersonic Free Shear Flows," *Annual Review of Fluid Mechanics*, Vol. 27, 1995, pp. 375–417.

[3]Bushnell, D. M., "Hypervelocity Scramjet Mixing Enhancement," *Journal of Propulsion and Power*, Vol. 11, No. 5, 1995, pp. 1088–1090.

[4]Bogdanoff, D., "Advanced Injection and Mixing Techniques for Scramjet Combustors," *Journal of Propulsion and Power*, Vol. 10, No. 2, 1994, pp. 183–190.

[5]Marble, F., Zukoski, E., Jacobs, J., Hendricks, G., and Waitz, I., "Shock Enhancement and Control of Hypersonic Mixing and Combustion," AIAA Paper 90-1981, 1990.

[6]Davis, D., and Hingst, W., "Progress Toward Synergistic Hypermixing Nozzles," AIAA Paper 91-2264, 1991.

[7]Waitz, I., Marble, F., and Zukoski, E., "An Investigation of a Contoured Wall Injector for Hypervelocity Mixing Augmentation," AIAA Paper 91-2265, 1991.

[8]Waitz, I., Marble, F., and Zukoski, E., "Vorticity Generation by Contoured Wall Injectors," AIAA Paper 92-3550, 1992.

[9]Mays, R. B., Thomas, R. H., and Schetz, J. A., "Low Angle Injection into a Supersonic Flow," AIAA Paper 89-2461, July 1989.

[10]Lee, R. E., and Linevsky, M. J., "Shadowgraph Studies of Angular Injection of a Sonic Jet into a Mach 2.8 Supersonic Flow," AIAA Paper 90-1618, June 1990.

[11]Dimotakis, P. E., "Turbulent Mixing and Combustion," *High-Speed Flight Propulsion Systems*, edited by S. N. B. Murthy and E. T. Curran, Vol. 137, Progress in Aeronautics and Astronautics, AIAA, Washington, DC, 1991, Chap. 5.

[12]Lee, S.-H., Jeung, I.-S., and Yoon, Y., "Computational Investigation of Shock-Enhanced Mixing: Application to Circular Cross Section Combustor," *AIAA Journal*, Vol. 36, No. 11, 1998, pp. 2055–2062.

[13]Scherrer, D., Dessornes, O., Montmayeur, N., and Ferrandon, O., "Injection Studies in the French Hypersonic Technology Program," AIAA Paper 95-6096, 1995.

[14]Baurle, R. A., Alexopoulos, G. A., and Hassan, H. A., "Analysis of Supersonic Combustors with Swept Ramp Injectors," *Journal of Propulsion and Power*, Vol. 13, No. 2, 1997, pp. 327, 328.

[15]Wilcox, D. C., "Reassessment of the Scale Determining Equation for Advanced Turbulence Models," *AIAA Journal*, Vol. 26, No. 11, 1988, pp. 1299–1310.

[16]Sislian, J. P., "Equations of Motion and Two-Equation Turbulence Model for Plane or Axisymmetric Turbulent Flows in Body-Oriented Orthogonal Curvilinear Coordinates and Mass-Averaged Dependent Variables," NASA CR 3025, Jan. 1978.

[17]Krishnamurty, V. S., "Effect of Compressibility on the Turbulence Structure and Its Modelling," Ph.D. Dissertation, Dept. of Aerospace Engineering, Mechanics and Engineering Science, Univ. of Florida, Gainesville, FL, Dec. 1996.

[18]Coakley, T. J., Horstman, C. C., Marvin, J. G., Viegas, J. R., Bardina, J. E., Huang, P. G., and Kussoy, M. I., "Turbulence Compressibility Corrections," NASA TM 108827, May 1994.

[19]Wilcox, D. C., "Dilatation-Dissipation Corrections for Advanced Turbulence Models," *AIAA Journal*, Vol. 30, No. 11, 1992, pp. 2639–2646.

[20]McBride, B. J., and Reno, M. A., "Coefficients for Calculating Thermodynamic and Transport Properties of Individual Species," NASA TM 4513, Oct. 1993.

[21]Dixon-Lewis, G., "Computer Modelling of Combustor Reactions," *Combustion Chemistry*, edited by W. C. Gardiner, Springer-Verlag, New York, 1984.

[22]Papamoschou, D., and Roshko, A., "The Compressible Turbulent Shear Layer: An Experimental Study," *Journal of Fluid Mechanics*, Vol. 197, 1988, pp. 453–477.

[23]Roe, P. L., "Approximate Riemann Solvers, Parameter Vectors, and Difference Schemes," *Journal of Computational Physics*, Vol. 43, 1981, pp. 357–372.

[24]Yee, H. C., Klopfer, G. H., and Montagné, J.-L., "High-Resolution Shock-Capturing Schemes for Inviscid and Viscous Hypersonic Flows," *Journal of Computational Physics*, Vol. 88, 1990, pp. 31–61.

[25]Douglas, J., Jr., "On the Numerical Integration of $\partial^2 u/\partial x^2 + \partial^2 u/\partial y^2 = \partial u/\partial t$ by Implicit Methods," *Journal of the Society for Industrial and Applied Mathematics*, Vol. 3, 1955, pp. 42–65.

[26]Peaceman, D. W., and Rachford, H. H., "The Numerical Solution of Parabolic and Elliptic Differential Equations," *Journal of the Society for Industrial and Applied Mathematics*, Vol. 3, 1955, pp. 28–41.

[27]Chang, C.-L., and Merkle, C. L., "The Relation Between Flux Vector Splitting and Parabolized Schemes," *Journal of Computational Physics*, Vol. 80, 1989, pp. 344–361.

[28]Patankar, S. V., *Numerical Heat Transfer and Fluid Flow*, Hemisphere, New York, 1980, pp. 143–146.

[29]Batten, P., Leschziner, M. A., and Goldberg, U. C., "Average-State Jacobians and Implicit Methods for Compressible Viscous and Turbulent Flows," *Journal of Computational Physics*, Vol. 137, No. 1, 1997, pp. 38–78.

[30]Coakley, T. J., and Huang, P. G., "Turbulence Modeling for High-Speed Flows," AIAA Paper 92-04366, 1992.

[31]Wilcox, D. C., *Turbulence Modeling for CFD*, DCW Industries, La Cañada, CA, 1994.

[32]Donohue, J. M., McDaniel, J. C., and Haj-Hariri, H., "Experimental and Numerical Study of Swept Ramp Injection into a Supersonic Flowfield," *AIAA Journal*, Vol. 32, No. 9, 1994, pp. 1860–1867.

[33]Oberkampf, W. L., and Blottner, F. G., "Issues in Computational Fluid Dynamics Code Verification and Validation," *AIAA Journal*, Vol. 36, No. 5, 1998, pp. 687–695.

[34]Roache, P. J., "Verification of Codes and Calculations," *AIAA Journal*, Vol. 36, No. 5, 1998, pp. 696–702.

[35]Mao, M., Riggins, D. W., and McClinton, C. R., "Numerical Simulation of Transverse Fuel Injection," *Proceedings of the CFD Symposium on AeroPropulsion*, 1990, pp. 635–667.

[36]Lewis, B., and von Elbe, G., *Combustion, Flames and Explosions of Gases*, 3rd ed., Academic Press, Orlando, FL, 1987, pp. 705–708.

J. P. Gore
Associate Editor